RSC Advances

PAPER

View Article Online
View Journal | View Issue

Cite this: *RSC Adv.*, 2025, **15**, 13603

Metal-polydopamine coordinated coatings on titanium surface: enhancing corrosion resistance and biological property

Yu-kun Mei,[ab] Ya-wen Zhu,[ab] Yu-wen Wei,[ab] Shu-di Li,[ab] Xuan Zhou,[ab] Ya-nan Yao[ab] and Jing Qiu *[abc]

Previous studies on polydopamine (PDA)-modified titanium implants have primarily focused on single-metal-ion systems (*e.g.*, Ag^+, Cu^{2+}, or Zn^{2+}), while overlooking the interplay between corrosion resistance, antioxidant retention, and antimicrobial efficacy under clinically relevant oxidative conditions. Here, we present a comparative analysis of Ag-, Cu-, and Zn-integrated PDA coatings fabricated *via* a two-step coordination strategy, addressing these limitations through systematic multi-parameter evaluation. Unlike prior studies, this study reveals distinct metal-PDA interaction mechanisms: XPS/EDS analyses confirm Zn^{2+} and Cu^{2+} form coordination complexes with PDA's catechol groups, whereas Ag^+ undergoes reduction to metallic nanoparticles (Ag^0), leading to divergent ion-release profiles (Zn^{2+} > Cu^{2+} > Ag^+) and biofunctional outcomes. Electrochemical testing under H_2O_2-simulated oxidative stress demonstrates Zn-PDA coatings exhibit superior corrosion resistance (polarization resistance: 4330 *vs.* 3900 and 2850 kΩ cm^2 for Cu-PDA and Ag-PDA, respectively), while Ag-PDA achieves the highest antibacterial efficacy (>95% reduction against *S. aureus* and *E. coli*). Notably, Zn/Cu-PDA coatings retain >80% of PDA's intrinsic antioxidant capacity, in contrast to Ag-PDA, which exhibits significant antioxidant depletion due to redox interference. *In vivo* rat models further differentiate our approach: all coatings show comparable soft-tissue integration and systemic biosafety, contrasting with earlier reports of Ag-induced cytotoxicity. By elucidating metal-specific performance trade-offs and establishing a design framework to balance corrosion resistance, ROS scavenging, and antimicrobial activity, this work advances clinically adaptable strategies for enhancing peri-implant tissue stability.

Received 13th January 2025
Accepted 17th April 2025

DOI: 10.1039/d5ra00301f

rsc.li/rsc-advances

1. Introduction

Owing to their exceptional mechanical properties and favorable biocompatibility, titanium and titanium alloys have been widely used in oral implantology and orthopedic applications.[1,2] Despite the high success rates associated with titanium-based implants, their long-term survival remains a concern, with peri-implantitis identified as the most prevalent complication. Meta-analyses indicate that peri-implantitis prevalence ranges from 20% to 22%.[3] Notably, the timely establishment and sustained maintenance of soft tissue integration (STI) across the mucosal interface are paramount for the success of implant-supported prostheses.[4,5]

Unlike natural teeth, the soft tissue attachment around implant abutments is inherently fragile due to compromised biological bonding and mechanical connections. The oral cavity, a dynamic biochemical environment, subjects dental materials to corrosion *via* interactions with body fluids, electrochemical activity (cathodic/anodic behavior), and microbial colonization, accelerating the degradation of titanium's passivation layer. This corrosion leads to increased metal ion release, disrupting tissue metabolism and contributing to implant failure.[6] Bacterial invasion and foreign bodies further exacerbate oxidative stress *via* reactive oxygen species (ROS) such as H_2O_2, which induces localized voltage differentials and elevates corrosion potential, even at low concentrations.[7] Over time, oxide film degradation releases metal ions and particles, accelerating corrosion, irritating tissues, and heightening failure risks.[8] Corrosion mechanisms in implants include mechanical, chemical/electrochemical, and frictional corrosion, with electrochemical corrosion predominating due to the multifactorial oral environment. These processes collectively challenge implant stability and longevity.[6,9,10]

Chemical surface modification techniques (*e.g.*, SAMs, silylation, Langmuir–Blodgett deposition) are widely used but limited by substrate specificity, complex instrumentation, and scalability issues.[11–13] Inspired by mussel adhesion mechanisms, polydopamine (PDA) coatings—pioneered by Lee *et al.*—

[a]*Department of Oral Implantology, Affiliated Stomatological Hospital of Nanjing Medical University, 1# Shanghai Road, Nanjing 210029, China. E-mail: qiujing@njmu.edu.cn*

[b]*Jiangsu Province Key Laboratory of Oral Diseases, Nanjing, China*

[c]*Jiangsu Province Engineering Research Center of Stomatological Translational Medicine, Nanjing, China*

offer a substrate-independent solution. Immersing substrates in dopamine solutions buffered to marine pH triggers spontaneous polymerization, forming stable, adhesive films *via* covalent/non-covalent interactions.[14,15]

PDA coatings feature reactive catechol groups, enabling multifunctional applications: (1) grafting bioactive molecules for tailored functionality; (2) chelating metal ions to construct metal-composite coatings (*e.g.*, titanium surfaces); and (3) exhibiting antioxidant properties and high photothermal efficiency. Their broad adhesion, stability, and versatility make them promising for advanced materials in biomedical, environmental, and engineering fields.[16,17]

In previous studies, PDA coatings enhance corrosion resistance in metallic implants by forming protective, hydrophilic layers. For example, PDA-modified magnesium alloys reduce corrosion *via* biomimetic hydroxyapatite (HA) mineralization, while titanium implants utilize Ce^{3+}–PDA interfaces to scavenge ROS and mitigate oxidative stress.[18] Aluminum alloys achieve self-healing through pH-responsive ZnMg MOF-LDH formation.[19] Antibacterial functionality is enabled by PDA-ferrocene coatings generating ROS (>95% efficacy against MRSA/*E. coli*), amplified to >99% eradication under NIR irradiation *via* photothermal-ROS synergy.[20] PDA coatings on PEEK with Ag/Cu ions sustain antimicrobial activity,[21] while PDA-hydrogels on HDPE reduce bacterial adhesion by 98% *via* hydrophilicity.[22]

Metal ion integration further extends PDA's versatility: Sr^{2+}-doped coatings promote osteogenesis,[18] Ag^{+} layers offer dual antibacterial/corrosion resistance,[21] and CeO_2-PDA heterostructures balance pH-responsive corrosion inhibition with ROS scavenging.[23] PDA's catechol/amine groups enable chelation (Fe^{3+}, Cu^{2+}) for tailored therapeutic release, highlighting its multifunctional potential in biomedical applications.[23]

Ag, Cu, and Zn are widely used in medical applications for their antimicrobial properties. Ag exhibits the strongest broad-spectrum activity, acting *via* ionic release and direct "contact sterilization".[24] Cu, an essential trace element, penetrates bacterial membranes through ion channels, disrupting enzyme activity and DNA synthesis.[25,26] Zn, though less potent, offers advantages such as safety, minimal side effects, and sustained antimicrobial effects by compromising membrane integrity and protein function.[27] However, their cytotoxicity and concentration-dependent efficacy remain challenges for clinical translation.

In this study, titanium surfaces were modified by employing a metal-polydopamine coordination strategy to assess the effects of different metal ions on the corrosion resistance of polydopamine coatings. Furthermore, the antioxidant and antibacterial properties of each coating were systematically evaluated. This investigation aims to establish a novel methodology for the modification of implant abutments, thereby enhancing their functional performance in clinical settings.

2. Materials and methods

2.1. Sample preparation

The commercially pure titanium (cpTi) specimens (Grade I, Baoji Titanium, China) were sequentially polished using silicon carbide abrasive paper (#600, #800, #1000, #1200), rinsed with deionized water, and air-dried prior to use. Then the titanium specimens were immersed in 2 mg per mL dopamine hydrochloride solution for 24 h, rinsed with double-distilled water and air-dried naturally to obtain the commercially pure titanium-polydopamine-coated (cpTi-PDA) specimens. Afterwards, commercially pure titanium-polydopamine-silver/copper/zinc ionic coating (cpTi-PDA-Ag/Cu/Zn) specimens were prepared by a "two-step" method. On the basis of the cpTi-PDA, each group of specimens was immersed in the same concentration of silver, copper and zinc sulphate solutions prepared with double-distilled water for 6 h, then rinsed with double-distilled water and air dried after taking out. Five groups of specimens, cpTi, cpTi-PDA, cpTi-PDA-Ag, cpTi-PDA-Cu, cpTi-PDA-Zn were obtained.

2.2. Surface characterization of the specimens

The surface micromorphology of the specimens was examined using a Scanning Electron Microscope (SEM, MAIA3, TESCAN, Czech Republic) at magnifications of 500× and 5000×, with an accelerating voltage of 20.0 kV. Selected images were analyzed for surface element distribution using an Energy Dispersive Spectrometer (EDS, TESCAN, Czech Republic). Five groups of specimens (cpTi, cpTi-PDA, cpTi-PDA-Ag, cpTi-PDA-Cu, cpTi-PDA-Zn) were randomly chosen to assess elemental compositions and chemical states *via* X-ray Photoelectron Spectroscopy (XPS, Thermo Scientific Escalab 250Xi, USA). Reference binding energies were determined using the National Institute of Standards and Technology XPS online database. The XPS spectra were calibrated to the binding energy of C 1s from adventitious carbon (284.8 eV). Data analysis was conducted using CasaXPS and Origin 2021 software, with experiments performed on three separate titanium disks.

2.3. Ion release assay

To detect metal ion release, five specimen groups (cpTi, cpTi-PDA, cpTi-PDA-Ag, cpTi-PDA-Cu, cpTi-PDA-Zn) were randomly selected and immersed in Fusayama's artificial saliva at pH 6.8 and 37 °C for varying durations (1, 3, 5, and 7 days).[28] At specified intervals, the extracts were analyzed using Inductively Coupled Plasma Mass Spectrometry (ICP-MS, PerkinElmer, USA). The measurement conditions include the following parameters: the inductively coupled plasma (ICP) was operated at an RF power of 1550 W with a coolant gas flow rate of 18 L min^{-1}, an auxiliary gas flow rate of 1.2 L min^{-1}, and a nebulizer gas flow rate of 1.08 L min^{-1}. The analysis utilized a resolution of 0.7 ± 0.1 u at 10% peak height, performed in peak jumping mode with 3 points per peak and an integration time of 0.1 s per point. For the mass spectrometer settings, the vacuum chamber pressure was maintained at 6.58×10^{4} Torr, while the quadrupole ion deflector (QID) was configured with a deflection voltage of −10 V and an RF voltage of 200 V. These conditions collectively ensured optimized instrument performance for the experimental measurements.

2.4. Surface hydrophilicity assay

The water contact angle test used the static drop method. Three specimens (cpTi, cpTi-PDA, cpTi-PDA-Ag, cpTi-PDA-Cu, cpTi-

PDA-Zn), each 5 mm in diameter, were randomly selected. A 2 μL drop of distilled water was placed on the specimen surfaces and observed after 5 seconds using a contact angle meter (JC2000C1, POWEREACH, China). The water contact angle for each specimen group was measured with the contact angle instrument.

2.5. Electrochemical corrosion test

Five groups of six specimens, each 15 mm in diameter (cpTi, cpTi-PDA, cpTi-PDA-Ag, cpTi-PDA-Cu, cpTi-PDA-Zn), were selected and mounted in self-curing epoxy resin, exposing 1 cm^2 coated surfaces. The specimens were cleaned with ethanol and deionized water before testing. Corrosion testing was performed using an electrochemical potentiostat (CS310H, Wuhan Corrtest Instrument Co., Ltd, China), with the specimens as the working electrode, a platinum wire as the auxiliary electrode, and Ag/AgCl as the reference electrode. Normal and 30 mM H_2O_2 artificial saliva were used to simulate standard and oxidized intraoral environments.[29] Tests were conducted in triplicate at 37 °C.

Each specimen stabilized at open-circuit potential (E_{corr}) for 2 hours before applying a 10 mV sinusoidal potential across frequencies from 1000 kHz to 10 mHz. Electrochemical impedance spectroscopy (EIS) measurements were performed using CS Studio5 software, and data such as Nyquist, Bode impedance, and Bode phase plots were analyzed and fitted with equivalent circuits using ZSimpWin software.

2.6. Cell culture

The L-929 cells were obtained from the Chinese Academy of Sciences Cell Bank (Shanghai, China). They were thawed in a complete medium consisting of Dulbecco's Modified Eagle's Medium (DMEM, Gibco, USA) with 10% Fetal Bovine Serum (FBS, Gibco, USA) and 1% penicillin/streptomycin (Gibco, USA). The cells were cultured in an incubator at 37 °C with 95% relative humidity and 5% CO_2. Cell growth was monitored regularly, and passaging occurred at 80% confluence.

2.7. Cell adhesion and proliferation assay

Five specimen groups (cpTi, cpTi-PDA, cpTi-PDA-Ag, cpTi-PDA-Cu, cpTi-PDA-Zn) were placed in a 96-well plate, with 8×10^3 L-929 cells seeded in each well. After 8 hours, the culture medium was removed, and cells were washed three times with Phosphate Buffered Saline (PBS, Gibco, USA). They were then fixed with 4% paraformaldehyde for 30 minutes, permeabilized with Triton X-100 (Beyotime, China) for 10 minutes, and stained with Actin-Tracker Red-Rhodamine (Beyotime, China) for 30 minutes and DAPI (Beyotime, China) for 3 minutes. Cell adhesion was observed using an inverted fluorescence microscope (Leica Microsystems CMS GmbH, Wetzlar, Germany) at 200× and 400× magnification.

For cell proliferation, 5 mm diameter specimens were placed in 96-well plates, each inoculated with 3×10^3 L-929 cells. After 1, 2, and 3 days of culture, the medium was replaced with a 10% Counting Kit-8 (CCK-8, APExBIO, USA) reagent solution. After 2 hours of incubation, absorbance at 450 nm was measured using a multifunctional microplate reader.

2.8. Antioxidant test

2.8.1. DPPH radical scavenging assay. Three specimens (cpTi, cpTi-PDA, cpTi-PDA-Ag, cpTi-PDA-Cu, cpTi-PDA-Zn) with a diameter of 5 mm were randomly selected and immersed in the 2,2-diphenyl-1-picrylhydrazyl (DPPH) working solution, and then incubated at room temperature of 25 °C for 30 min, and then 300 μL was pipetted into a 96-well plate, and then adjusted to the zero with anhydrous alcohol, and then the absorbance values of the wells were measured at the wavelength of 517 nm. The absorbance of each well was determined (wavelength = 517 nm).

2.8.2. Intracellular ROS content. Five sets of 5 mm diameter specimens (cpTi, cpTi-PDA, cpTi-PDA-Ag, cpTi-PDA-Cu, cpTi-PDA-Zn) were placed in a 96-well plate with 3 replicate wells for each set. L-929 cells (3×10^3 per well) were inoculated into the 96-well plate and incubated in a cellular incubator for 24 h. The original medium was discarded. L-929 cells (3×10^3 per well) were inoculated into 96-well plates and incubated in a cellular thermostat for 24 h. The original medium was discarded, and the L-929 cells were incubated in complete medium containing 0.75 mM H_2O_2 for 2 h. The L-929 cells were rinsed twice with PBS after aspirating the medium to remove the residual reactive oxygen species and then incubated in complete medium with 10 μM DCHF-DA for 30 min in a protected environment against light. The images were acquired using a confocal laser microscope with an excitation wavelength of 488 nm and emission wavelength of >500 nm. Excitation wavelength of 488 nm and emission wavelength of > 500 nm.

2.9. *In vitro* antibacterial activity

The frozen *Staphylococcus aureus* (*S. aureus*, ATCC 25923) and *Escherichia coli* (*E. coli*, ATCC 25922) were carefully taken out in liquid nitrogen, and then rewarmed in a 37 °C water bath and centrifuged (1000 rpm, 5 min) on a flat surface, and the supernatant was discarded and added to fresh Luria-Bertani (LB) medium, and the bacteria were blown gently to mix. A small amount of the bacterial solution was dipped into a bacterial inoculation loop and placed in a shaking tube containing LB medium, and the bacteria were increased on a shaking table for 24 h. After several repetitions were made to obtain stable growth of the bacterial strains, the bacterial solution was configured into a bacterial suspension of 1×10^5 Colonies Formed Units (CFU) per mL by turbidimetric method for the following use.

2.9.1. Bacteria counting test. Five sets of specimens (cpTi, cpTi-PDA, cpTi-PDA-Ag, cpTi-PDA-Cu, cpTi-PDA-Zn) with a diameter of 15 mm were placed in a 24-well plate, and three replicate wells were set up for each set. Bacterial suspensions were added to each well. After 24 h of incubation, the original culture medium was aspirated, 1 mL of PBS was added to each well, rinsed gently, and new LB medium was added. After ultrasonic shaking for 10 min, an appropriate amount of bacterial suspension was diluted by 10^5. ach LB agar plate was

inoculated with 100 μL of diluted bacterial suspension, incubated at 37 °C, and each set of plates was counted using an automatic colony counter.

2.9.2. Live/dead fluorescence staining assay. The dye mixture was obtained appropriate amount of component A and component B from the Viable Dead Bacteria Viability Kit (Thermofisher, USA) and mixed well in the dark. Then per mL of bacterial suspension was added 3 μL of fuel mix, mixed thoroughly and stayed for 15 minutes at room temperature in the absence of light. 5 μL of stained bacterial suspension was aspirated in the center of a slide, the cover slip was sealed and images were collected using a laser scanning confocal microscope (Leica Microsystems, Wetzlar, Germany).

2.10. *In vivo* study

The implants were designed and divided into five groups, modified with the appropriate coatings on their gingival abutment portions, sterilized and sealed for use.

All animal experimental designs and procedures were approved by the Laboratory Animal Welfare Ethics Committee of Nanjing Medical University (Ethics No. 2310028) and followed the recommendations of the IACUC Guide. Sprague Dawley rats (gender = male, $n = 18$, weight = 200–300 g, age = 7 weeks) were purchased from the Medical Laboratory Animal Center of Nanjing Medical University. Briefly, the rats were randomly divided into five groups: cpTi, cpTi-PDA, cpTi-PDA-Ag, cpTi-PDA-Cu, and cpTi-PDA-Zn group. The surgical procedure is as follows: 2% (w/w) pentobarbital sodium sterile aqueous solution was injected intraperitoneally into the rats, and after their respiration was slowed down and general anesthesia was complete, the mouths of the rats were propped open with a cotter, and the maxillary first molars were exposed. After disinfecting the periphery of the operative area with an iodophor swab and local infiltration anesthesia of the surrounding gingiva with Primacaine, the gingiva was separated with a probe. After complete gingival separation, the molar was carefully extracted with an apical tappet along the perimeter of the maxillary first molar. An implant socket of 2 mm in diameter and 4 mm in depth was prepared in the extraction socket using a bur and rinsed and cooled with sterile saline.

After the preparations were completed, the abutments were implanted into the sockets according to the established grouping, and the rats were observed to make sure that their vital signs were stable and to wait for natural awakening. After surgery, the rats were routinely housed and fed a normal diet. The rats were euthanized at 1 week after surgery, and the soft tissue samples around the implants were circumcised with a 12-gauge blade. The thoracic and abdominal cavities were dissected, and the hearts, livers, spleens, lungs, and kidneys were removed and immediately immersed in 4% (w/w) paraformaldehyde solution for fixation.

The fixed samples were subjected to histological examination, and paraffin sections were firstly made using the conventional steps, which were briefly described as follows: ethanol gradient dehydration, xylene transparency, wax dipping, paraffin embedding, and sectioning. Paraffin sections of soft tissues surrounding the implants were examined and healing was evaluated by H&E and Masson's staining.

In addition, the rat organs including the heart, liver, kidney, lung and spleen were histologically evaluated to test the biosafety of the coating. Finally, H&E and Masson's staining were performed to observe the metabolism. The tissue samples were observed by an orthogonal microscope.

2.11. Statistical analysis

The data were processed using SPSS 22.0 software and analyzed through one-way ANOVA, followed by S–N–K multiple comparisons at a significance level of $\alpha = 0.05$. Differences were deemed statistically significant if $p < 0.05$.

3. Results and discussion

3.1. Fabrication and characterization of coating surface

The surface morphology of each group of specimens was observed by SEM (Fig. 1A). Under low magnification, there was no obvious difference between the specimens of each group. Under high magnification, the surface of the specimens in the cpTi group was relatively smooth, and the mechanical scratches after polishing were visible. Compared with the cpTi group, the surface of the cpTi-PDA group showed a uniform coating structure. On the surfaces of cpTi-PDA-Ag, cpTi-PDA-Cu and cpTi-PDA-Zn groups, scattered aggregates of nanospherical particles appeared on the coating structure. The surface distribution analysis of the corresponding planes by EDS (Fig. 1B) showed that the concentration of metal ions was high in the specimens of each group where the spherical particles are aggregated.

Moreover, XPS analysis was performed on the surfaces of five groups of specimens (Fig. 2A–E). The XPS wide scan spectra analysis in Fig. 2A showed that titanium (Ti), carbon (C), nitrogen (N), and oxygen (O) could be detected on the surfaces of the four groups of specimens. Additionally, Ag, Cu and Zn could be detected on the surfaces of the specimens of the cpTi-PDA-Ag, cpTi-PDA-Cu, and cpTi-PDA-Zn groups, respectively. Combined with the EDS analysis above, it showed that the corresponding metal ions had successfully bonded to the PDA coatings in all groups. Compared with the cpTi group, due to the loading of PDA coatings on the specimen surface, the Ti 2p and O 1s peaks of the cpTi-PDA, cpTi-PDA-Ag, cpTi-PDA-Cu, and cpTi-PDA-Zn groups showed a decreasing tendency, and the C 1s and N 1s peaks increased significantly. The presence of C and N on the surface of specimens in the cpTi group might be caused by air pollution.[30,31]

Fig. 2B showed the XPS high-resolution spectra analysis of Ag 3d, Cu 2p, and Zn 2p signals on the surface of specimens of cpTi-PDA-Ag, cpTi-PDA-Cu, and cpTi-PDA-Zn groups, respectively, and the results indicated that the metal ions of all the groups were reduced to different degrees due to the strong reducing property of PDA. The XPS analysis of Zn 2p, Cu 2p, and Ag 3d orbitals on the polydopamine (PDA)-modified titanium surface revealed distinct chemical states and interaction mechanisms: Zn^{2+} exhibited characteristic binding energies at

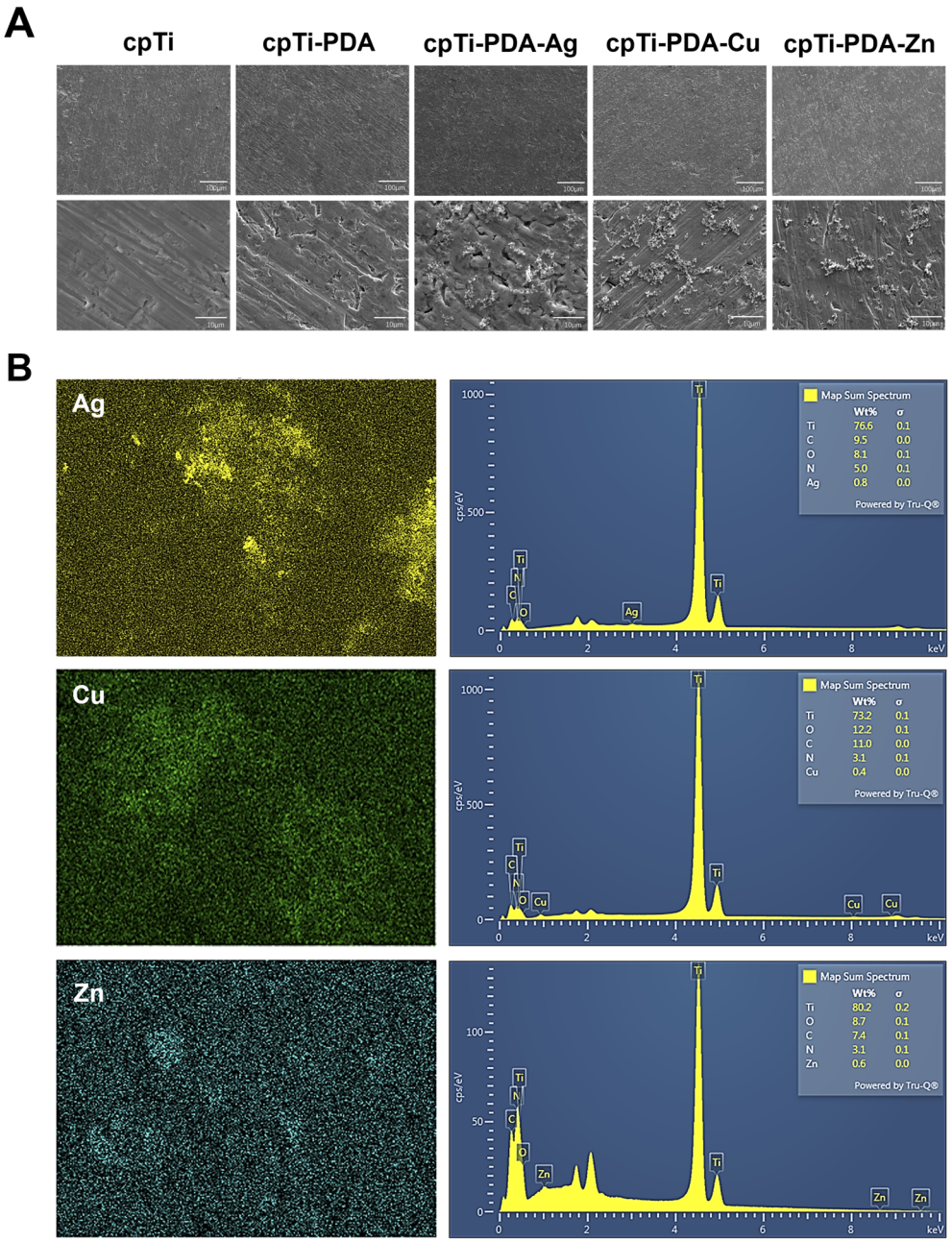

Fig. 1 Surface microstructures of the coatings. (A) Surface microstructures of different specimen surfaces. (B) Energy-dispersive X-ray mapping of the cpTi-PDA-Ag, cpTi-PDA-Cu and cpTi-PDA-Zn surface.

~1022–1023 eV (Zn $2p_{3/2}$) and ~1045 eV (Zn $2p_{1/2}$), confirming its oxidized state and strong coordination with oxygen/nitrogen-containing functional groups in PDA without detectable metallic Zn.[32,33] Cu^{2+} showed prominent peaks at ~933.5–934.5 eV (Cu $2p_{3/2}$) and ~953–954 eV (Cu $2p_{1/2}$), accompanied by intense satellite peaks indicative of a high-spin state, suggesting robust coordination with PDA's amino or hydroxyl groups, with no evidence of Cu^{+} or metallic Cu.[34] In contrast, Ag existed predominantly as metallic nanoparticles (Ag^0), evidenced by Ag $3d_{5/2}$ and $3d_{3/2}$ peaks at ~368.5 eV and ~374.5 eV, respectively, with a 6 eV splitting, reflecting weak interaction with PDA likely through physical adsorption or surface deposition and no detectable oxidized Ag species.[35,36] These findings highlighted PDA's ability to stabilize Zn^{2+} and Cu^{2+} through chemical coordination while accommodating Ag^0 nanoparticles, offering a foundation for designing multifunctional composites tailored to catalytic, electronic, or antimicrobial applications. Fig. 2C–E showed the XPS high-resolution spectra analysis of Ti 2p, C 1s, and O 1s signals. According to the XPS online database, Ti $2p_{3/2}$ (458.6 eV) and Ti $2p_{1/2}$ (464.5 eV) were attached to TiO_2, and Ti $2p_{3/2}$ (453.7 eV) was attached to the Ti base in the inner layer of TiO_2.[30] After loading PDA coatings, the Ti 2p peaks of cpTi-PDA group, cpTi-PDA-Ag group, cpTi-PDA-Cu group, and cpTi-PDA-Zn group showed significant decrease, while C–C (284.8 eV),

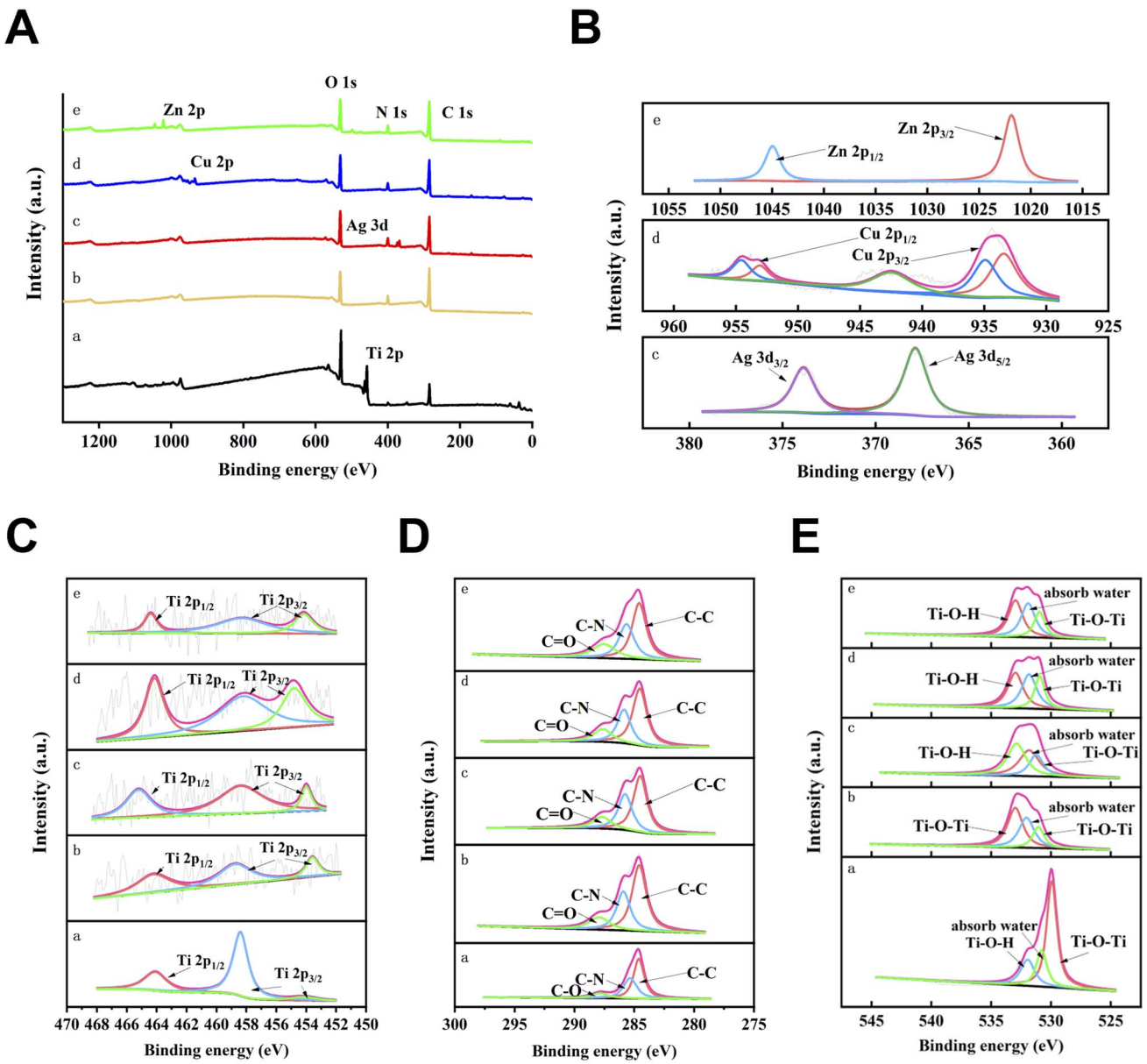

Fig. 2 Surface elemental analysis of various groups of specimens. (A) XPS wide scan spectra analysis; (B–E) XPS high-resolution spectra analysis of Zn 2p, Cu 2p, Ag 3d, Ti 2p, C 1s, and O 1s peaks. The letters a–e correspond in turn to cpTi, cpTi-PDA, cpTi-PDA-Ag, cpTi-PDA-Cu, and cpTi-PDA-Zn.

C–N (286 eV), and C–O (287.7 eV) showed significant increase, and Ti–O–Ti (530 eV) showed significant decrease.[37]

ICP-MS was used to measure the release of metal ions from the leachate of cpTi-PDA-Ag, cpTi-PDA-Cu, and cpTi-PDA-Zn specimens after immersion in artificial saliva at 37 °C for 1, 3, 5, and 7 days (Fig. 3C). It could be seen that all three groups of specimens had metal ion release, among which the silver ion release was the lowest, the release of zinc ion on the first day was lower than that of copper ion, and the release was higher than that of copper ion on 3, 5 and 7 d. The release of zinc ion was also higher than that of copper ion.

The hydrophilicity of the specimen surface was expressed by the size of the water contact angle, the smaller the water contact angle, the better the hydrophilicity of the material surface. As shown in Fig. 3A and B, the water contact angles of cpTi-PDA-Cu were smallest, and the water contact angles of the cpTi-PDA-Zn group were not statistically different from those of the cpTi-PDA-Cu group. It showed that the PDA coating could enhance the hydrophilicity of the titanium surface, and the introduction of metal ions played an enhanced role.

In this part of the study, we fabricated PDA coatings on titanium surfaces, capitalizing on the strong adhesion properties inherent to PDA. The resultant coatings demonstrated exceptional physicochemical properties, consistent with findings reported in the existing literature.[33] Additionally, employing a metal-polydopamine coordination strategy, we synthesized cpTi-PDA-Ag, cpTi-PDA-Cu, and cpTi-PDA-Zn. The efficient binding of the respective metal ions to the PDA

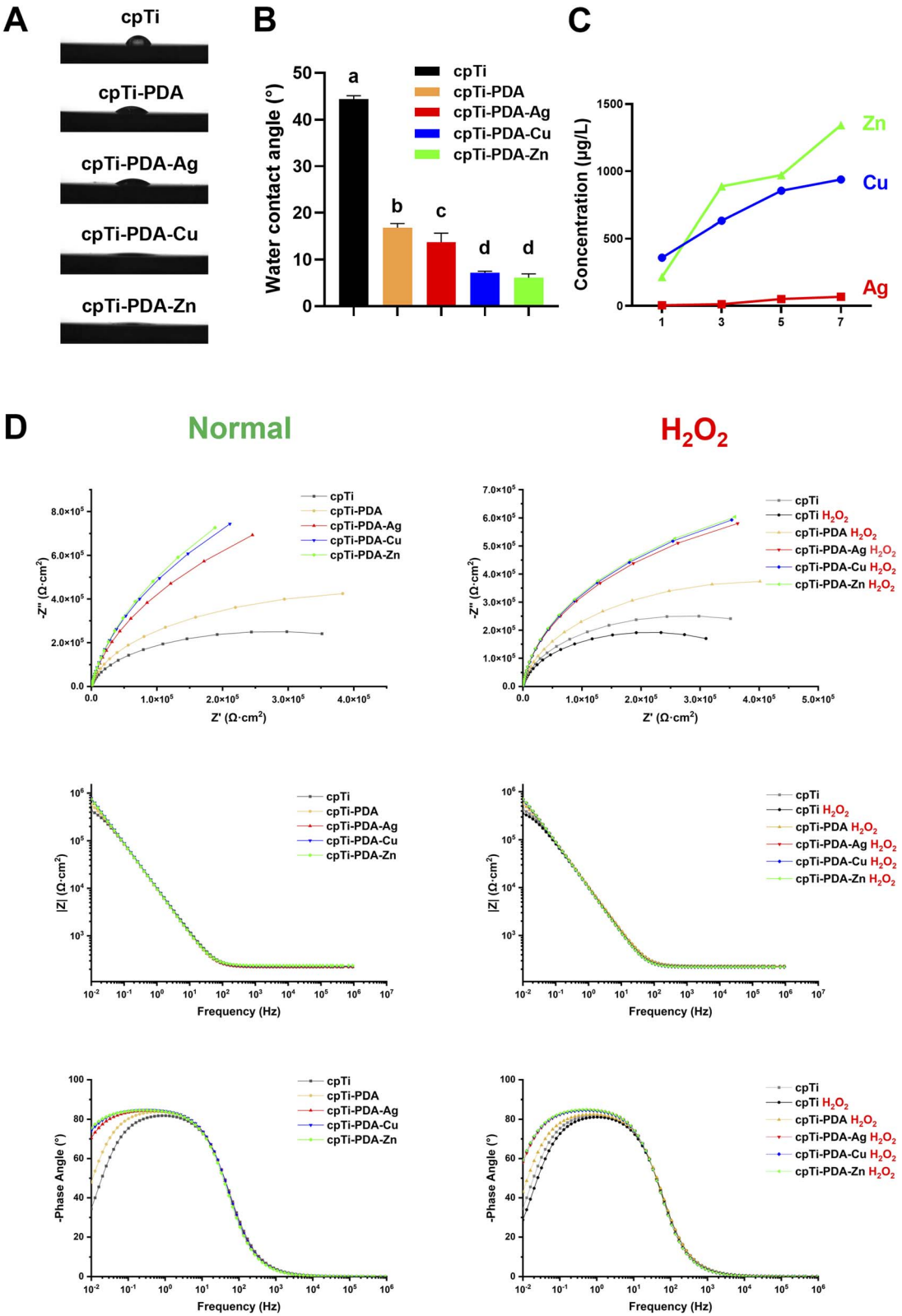

Fig. 3 Coating characterisation and corrosion resistance testing. (A) Water contact angle test charts for each group of specimens. (B) Water contact angle data for each group of specimens. (C) Release curves of metal ions from cpTi-PDA-Ag, cpTi-PDA-Cu, cpTi-PDA-Zn specimens after different immersion times. (D) Electrochemical impedance spectra of each specimen under different conditions. (i) Nyquist plots; (ii) Bode impedance plots; (iii) Bode phase plots. Data are expressed as means ± SD, with $n = 3$. Bars labeled with different letters denote statistically significant differences ($p < 0.05$).

coatings was confirmed through EDS and XPS. The ICP-MS results demonstrated significantly higher release of Zn^{2+} and Cu^{2+} ions from their respective complexes compared to Ag^{+} ions. These findings collectively indicated that Ag^{+} ions were preferentially reduced to Ag^{+} nanoparticles by polydopamine through redox processes, in contrast to Zn^{2+} and Cu^{2+} ions which primarily interact with the polymer *via* coordination-based complexation mechanisms, as evidenced by XPS analysis. The hydrophilicity of the coating surface was significantly enhanced through the incorporation of metal ions with PDA, as evidenced by water contact angle measurements. This increase in hydrophilicity is vital for soft tissue attachment. Hydrophilic surfaces facilitate tighter soft tissue attachment compared to their hydrophobic counterparts.[38]

3.2. Electrochemical impedance spectroscopy

The representative EIS spectra obtained from the electrochemical corrosion tests on each group of specimens using artificial saliva as the electrolyte was shown in Fig. 3D, and the specimens were categorized into the normal group and the H_2O_2 group according to whether or not H_2O_2 was added to the artificial saliva. The Nyquist plots could be seen in that the curves of each group of specimens showed capacitive resistance arcs with different radii. The cpTi group had the smallest radius among the normal group, and the radius of cpTi-PDA group increased after loading the PDA coating, and the radius of cpTi-PDA-Ag, cpTi-PDA-Cu, cpTi-PDA-Zn group continued to increase after further adding of metal ions to PDA coating. The size of the arc resistance radius is proportional to the corrosion resistance of the corresponding material, *i.e.*, the larger the radius, the better the corrosion resistance. The phase angle can be used to assess the integrity of the surface structure of a material, a higher phase angle suggests a more stable surface structure.[39] At the lowest frequency of 0.01 Hz, the phase angle of the cpTi group dropped below 40°, the phase angle of the cpTi-PDA group ranged from 40° to 60°, and the phase angle of the other three groups ranged from 70° to 80°. The Bode impedance diagram showed the absolute values of the impedance of each group of specimens in artificial saliva in the corresponding frequency band, among which the cpTi-PDA-Zn group had the highest impedance amplitude in the low-frequency region, indicating that the corresponding specimens had the strongest corrosion resistance. It could be seen that the results of the three electrochemical impedance spectra were consistent. Compared with the H_2O_2 group, the corrosion resistance of the specimens in the oxidized environment decreased, but the strength of the corrosion resistance did not change among the specimens in each group.

The EIS data were fitted using optimized equivalent circuit models to quantify the corrosion resistance of cpTi and modified specimens (Table 1). For cpTi and cpTi H_2O_2 groups, the R(QR) circuit ($R_s(R_{ct}Q_{dl})$) yielded excellent agreement with experimental data ($\chi^2 \leq 1.0 \times 10^{-3}$),[40,41] where R_s (solution resistance) increased from $12.5 \pm 0.5\ \Omega\ cm^2$ (cpTi) to $18.3 \pm 0.8\ \Omega\ cm^2$ (cpTi H_2O_2), consistent with the reduced ionic mobility in H_2O_2-containing artificial saliva. The charge transfer resistance (R_{ct}) decreased by 23% for cpTi in H_2O_2 (560 ± 20 *vs.* $430 \pm 50\ k\Omega\ cm^2$), confirming H_2O_2-induced corrosion acceleration.

For PDA-coated groups, the hierarchical R(Q(R(QR))) circuit ($R_s(Q_f(R_f(Q_{dl}R_{ct})))$) resolved the contributions of the PDA-metal composite layer (R_f) and substrate interface (R_{ct}).[40] The total polarization resistance ($R_p = R_f + R_{ct}$) ranked as cpTi-PDA-Zn ($4330\ k\Omega\ cm^2$) > cpTi-PDA-Cu ($3900\ k\Omega\ cm^2$) > cpTi-PDA-Ag ($2850\ k\Omega\ cm^2$), demonstrating Zn^{2+} doping's superior barrier effect. Exposure to H_2O_2 reduced R_{ct} by 20–62% across all groups (*e.g.*, cpTi-PDA-Zn: $2130 \pm 60 \rightarrow 810 \pm 80\ k\Omega\ cm^2$), yet cpTi-PDA-Zn retained the highest R_p ($1660\ k\Omega\ cm^2$), 2.1× greater than cpTi-PDA-Ag H_2O_2. The near-ideal CPE dispersion indices ($n = 0.89$–0.96) and low χ^2 values ($\leq 1.0 \times 10^{-3}$) validated the models' reliability. This analysis confirms that PDA coatings synergize with metal-ion doping (Zn > Cu > Ag) to enhance corrosion resistance, with cpTi-PDA-Zn exhibiting optimal performance in both oxidative and non-oxidative environments.

EIS serves as a "quasi-steady-state" detection method, preserving the surface properties of the material under investigation.[42,43] Utilizing EIS in conjunction with fitting analysis, we found that the incorporation of metal ions significantly enhanced the corrosion resistance of PDA coatings. This improvement might be attributed to the stabilization of the PDA matrix by metal ions, as well as inherent differences in corrosion resistance among various metal elements. Prior studies indicated that PDA could form 1 : 1 and 1 : 2 metal-polydopamine complexes with transition metal ions,

Table 1 Impedance parameter values of different coatings exposed to artificial saliva with or without H_2O_2

Cluster	Equivalent circuit	R_s ($\Omega\ cm^2$)	Q_f ($\mu F\ s^{n-1}\ cm^{-2}$)	n (Q_f)	R_f ($k\Omega\ cm^2$)	Q_{dl} ($\mu F\ s^{n-1}\ cm^{-2}$)	n (Q_{dl})	R_{ct} ($k\Omega\ cm^2$)	χ^2 ($\times 10^{-3}$)
cpTi	R(QR)	12.5 ± 0.5	—	—	—	1.774	0.94	560 ± 20	1.0
cpTi-PDA	R(Q(R(QR)))	14.2 ± 0.6	8.5×10^{-3}	0.92	300 ± 10	1.807	0.95	630 ± 30	1.0
cpTi-PDA-Ag	R(Q(R(QR)))	15.8 ± 0.7	11.2×10^{-3}	0.91	1200 ± 60	1.774	0.95	1650 ± 90	1.0
cpTi-PDA-Cu	R(Q(R(QR)))	13.9 ± 0.5	9.6×10^{-3}	0.93	1800 ± 50	1.731	0.95	2100 ± 80	1.0
cpTi-PDA-Zn	R(Q(R(QR)))	13.1 ± 0.4	10.5×10^{-3}	0.94	2200 ± 40	1.785	0.95	2130 ± 60	1.0
cpTi H_2O_2	R(QR)	18.3 ± 0.8	—	—	—	1.794	0.93	430 ± 50	1.0
cpTi-PDA H_2O_2	R(Q(R(QR)))	20.1 ± 0.9	7.8×10^{-3}	0.89	220 ± 20	1.763	0.91	520 ± 60	1.0
cpTi-PDA-Ag H_2O_2	R(Q(R(QR)))	22.5 ± 1.0	9.5×10^{-3}	0.90	650 ± 40	1.745	0.96	760 ± 70	1.0
cpTi-PDA-Cu H_2O_2	R(Q(R(QR)))	21.7 ± 1.1	8.8×10^{-3}	0.92	750 ± 30	1.752	0.96	790 ± 50	1.0
cpTi-PDA-Zn H_2O_2	R(Q(R(QR)))	19.6 ± 0.9	10.2×10^{-3}	0.93	850 ± 50	1.736	0.96	810 ± 80	1.0

suggesting that the differential binding affinities of distinct metal ions to polydopamine might play a crucial role in conferring enhanced corrosion resistance to the coatings.[44]

Surface coatings improve corrosion resistance in biodegradable implants *via* diverse mechanisms. Chemical conversion coatings (phosphate, fluoride, rare-earth) create dense oxide/hydroxide layers (*e.g.*, MgO, Ca–P) that physically block corrosive agents.[45] Micro-arc oxidation (MAO) produces porous ceramic layers (*e.g.*, $MgAl_2O_4$), though porosity necessitates polymer sealing to prevent electrolyte infiltration.[46] Hybrid organic–inorganic systems (polydopamine/HA, PLGA/graphene) combine barrier effects, chemical inhibition, and tunable degradation.[47] However, single-layer coatings face limitations: chemical coatings exhibit non-uniform adhesion due to processing variability, while superhydrophobic biomimetic coatings lack mechanical durability.[48]

Balancing corrosion protection with biofunctionality remains critical. Defects in graphene coatings require functionalization to harmonize impermeability and biocompatibility.[48] Drug-eluting coatings (*e.g.*, Ag nanoparticles, antibiotics) combat microbial corrosion but may accelerate galvanic degradation.[47] Nanotubular structures (*e.g.*, TiO_2) enhance osseointegration *via* bioactive molecule loading (BMP-2, NAC) but risk localized corrosion due to high surface area.[49] Future strategies focus on multifunctional hybrid architectures

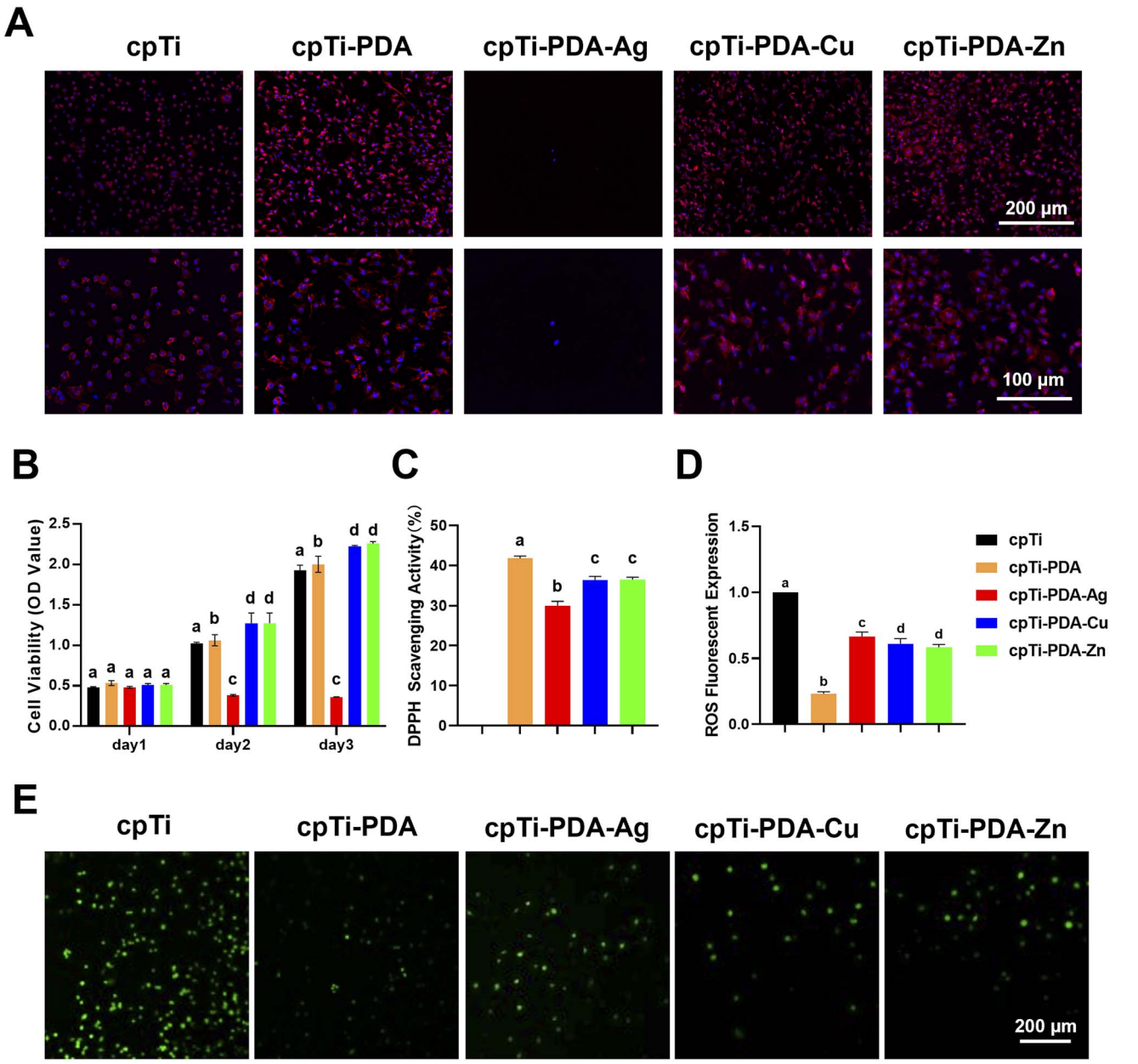

Fig. 4 *In vitro* cellular assays and antioxidant investigation. (A) Adhesion capacity of L-929 cells on the surface of specimens in each group. (B) Proliferative activity of L-929 cells on the surface of specimens in each group. (C) DPPH free radical scavenging rate; (D and E) L-929 intracellular reactive oxygen species detection. Data are expressed as means ± SD, with $n = 3$. Bars labeled with different letters denote statistically significant differences ($p < 0.05$).

(*e.g.*, MAO-polymer bilayers) that integrate corrosion resistance, bioactive drug delivery, and osteogenic properties. Optimizing biodegradable polymer compositions and gradient designs is essential to synchronize degradation with tissue regeneration.[48]

3.3. Cell adhesion and cell proliferation

After 8 hours of incubation, the morphology of L-929 cells adhering to cpTi, cpTi-PDA, cpTi-PDA-Ag, cpTi-PDA-Cu and cpTi-PDA-Zn surfaces were observed (Fig. 4A). At low magnification, the cpTi-PDA-Ag surface had the least number of adherent cells. Compared to cpTi, at high magnification, the cytoskeleton of cpTi-PDA, cpTi-PDA-Cu and cpTi-PDA-Zn surfaces was outspread and had a larger spreading area.

The proliferation activity of L-929 cells on the surface of each group of specimens was shown in Fig. 4B. On the first day, each group of specimens showed similar cell proliferation rate, and then the cell proliferation rate of the cpTi-PDA-Ag group decreased significantly on the second two days, while the cell proliferation rate of the cpTi-PDA-Cu, and cpTi-PDA-Zn groups were better than cpTi-PDA group, and the rates of the two groups were similar.

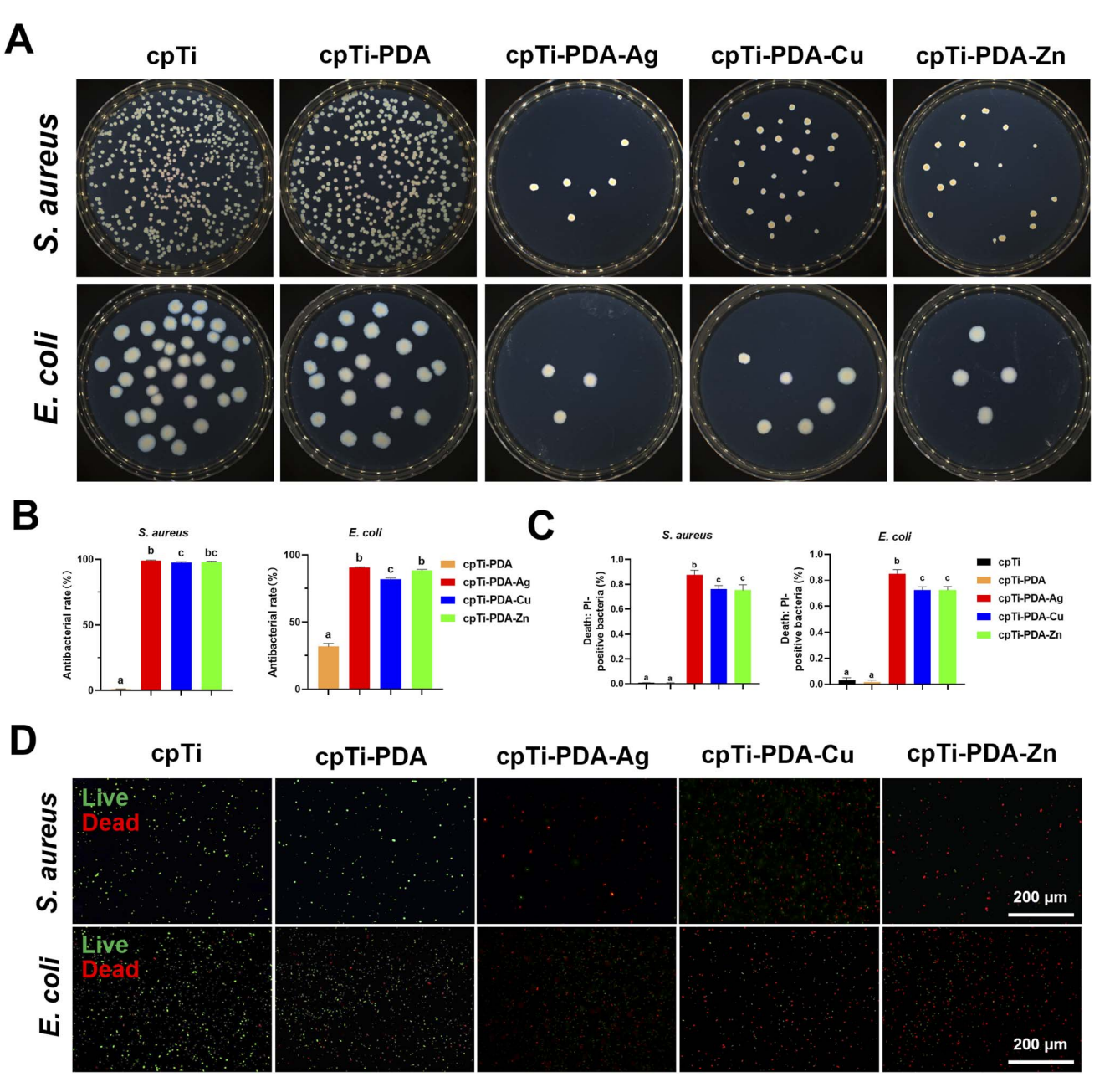

Fig. 5 Test of *in vitro* antibacterial effects. (A and B) Surface viable bacterial colony count and antimicrobial rate analysis of each group of specimens. (C and D) Live–dead bacterial staining of *S. aureus* and *E. coli* on the surface of specimens in each group and death: PI-positive bacteria of each group of specimens. Data are expressed as means ± SD, with $n = 3$. Bars labeled with different letters denote statistically significant differences ($p < 0.05$).

From this part, PDA enhances cell adhesion on the material surface and improves the biocompatibility of the material surface, which has been demonstrated in previous studies.[50,51] Meanwhile, the introduction of beneficial metal ions also played a positive role. In contrast, Ag exhibits greater biotoxicity, which tells us we need to load it in a better way.

3.4. Antioxidant and antimicrobial capacity of coatings

The antioxidant capacity was evaluated through the DPPH radical scavenging assay and the ROS scavenging rate in L-929 cells exposed to oxidative stress. As shown in Fig. 4C–E, the results revealed the following hierarchy of antioxidant efficacy: cpTi-PDA had the highest efficacy, followed by cpTi-PDA-Zn and cpTi-PDA-Cu, which were similar, and cpTi-PDA-Ag had the lowest efficacy. This pattern might be ascribed to the pronounced oxidizing properties of the metal ions. Importantly, the antioxidant activity of PDA was preserved to a certain extent, likely due to ligand-binding interactions between the metal ions and the polydopamine matrix.

Fig. 5A and B showed the results of the plate colony counts on the surface of each specimen, as well as the inhibition rate calculated by the formula. Fig. 5C and D showed the staining results of live and dead bacteria, in which the live bacteria matched green fluorescence under the microscope and the dead bacteria matched red fluorescence under the microscope. It could be seen that cpTi-PDA-Ag, cpTi-PDA-Cu and cpTi-PDA-Zn groups had strong antibacterial ability.

Bacterial invasion and ROS generated by the inflammatory response are two major challenges affecting the stability of the implant abutment-soft tissue interface. Bacterial invasion is among the foremost contributors to peri-implantitis. The

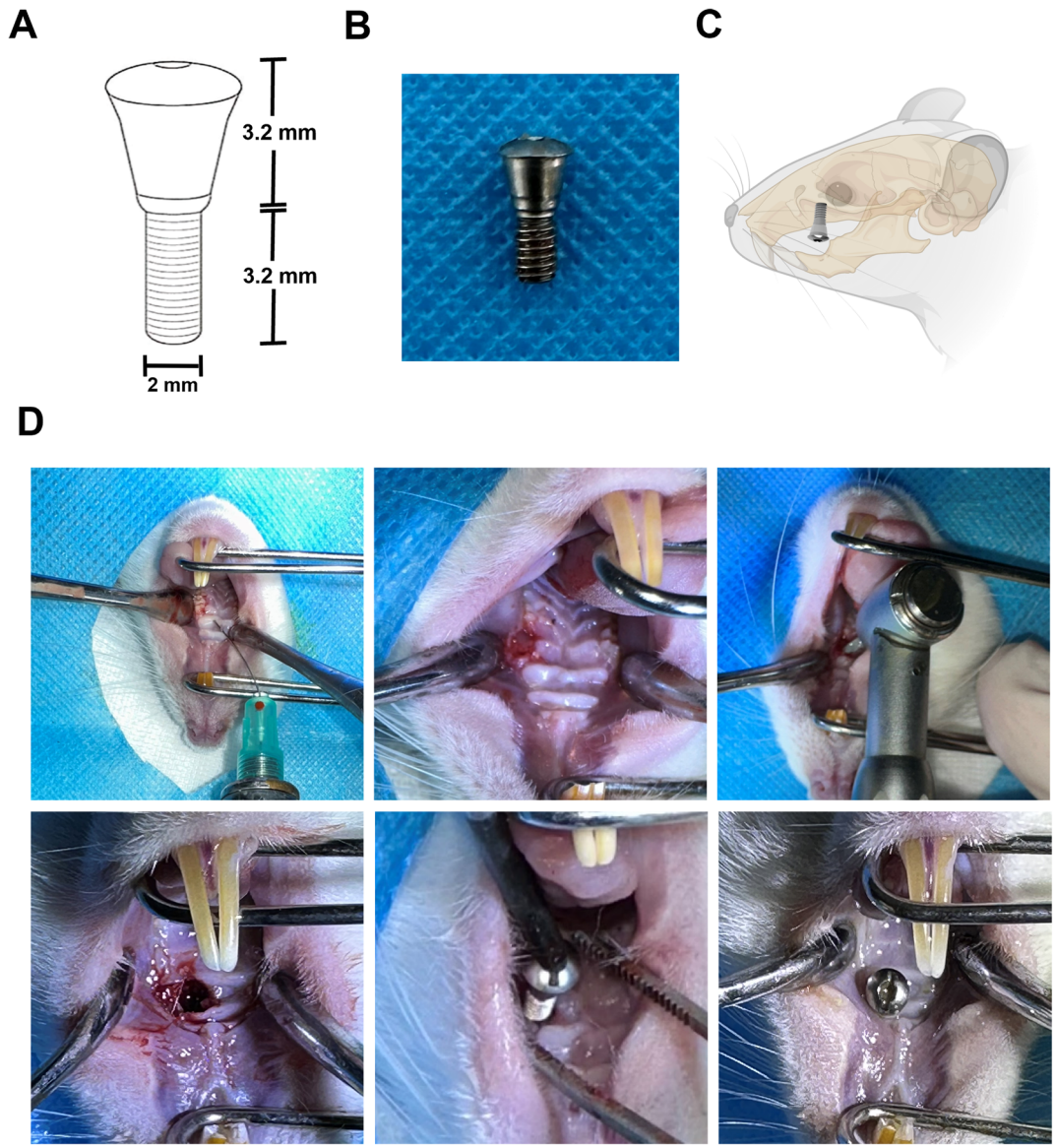

Fig. 6 Dental implant design and surgical schematic. (A) Dental implant size. (B) Image of dental implant. (C) Surgery diagram. (D) Surgical procedure for constructing a rat maxillary first molar immediate implant model.

proliferation of bacteria subsequently amplifies the inflammatory response, resulting in increased ROS production, which can inflict damage on surrounding tissues. Therefore, strategies aimed at reducing bacterial adhesion to the implant surface and limiting excessive ROS generation in the early postoperative period are essential for promoting long-term implant success.[52] In pursuit of a synergistic approach that encompasses both antibacterial and antioxidant properties, we systematically evaluated the antioxidant capacity of the surface coatings applied to each group of samples. For the antimicrobial evaluation, we specifically selected Gram-positive *S. aureus* and Gram-negative *E. coli* as target species.

PDA has emerged as a promising antimicrobial material, characterized by its exceptional photothermal conversion efficiency and the presence of abundant catechol and sec-amine functional groups. The hydrogen peroxide generated by PDA can denature proteins in bacterial cell membranes, disrupting membrane integrity and leading to bacterial cell death, thereby establishing PDA as an innovative and effective bio-antimicrobial agent.[53–56] Additionally, the extensive range of chemical reaction sites available on PDA, combined with its mild preparation methods, has facilitated its application in the interfacial chemical modification of antimicrobial composites. For example, silver ions can be *in situ* reduced on the PDA surface to form antimicrobial silver nanoparticles (AgNPs), thus creating effective antimicrobial interfaces.[57] In the present study, we evaluated the antibacterial properties of three commonly used medical metal ions: Ag, Cu and Zn. Viable

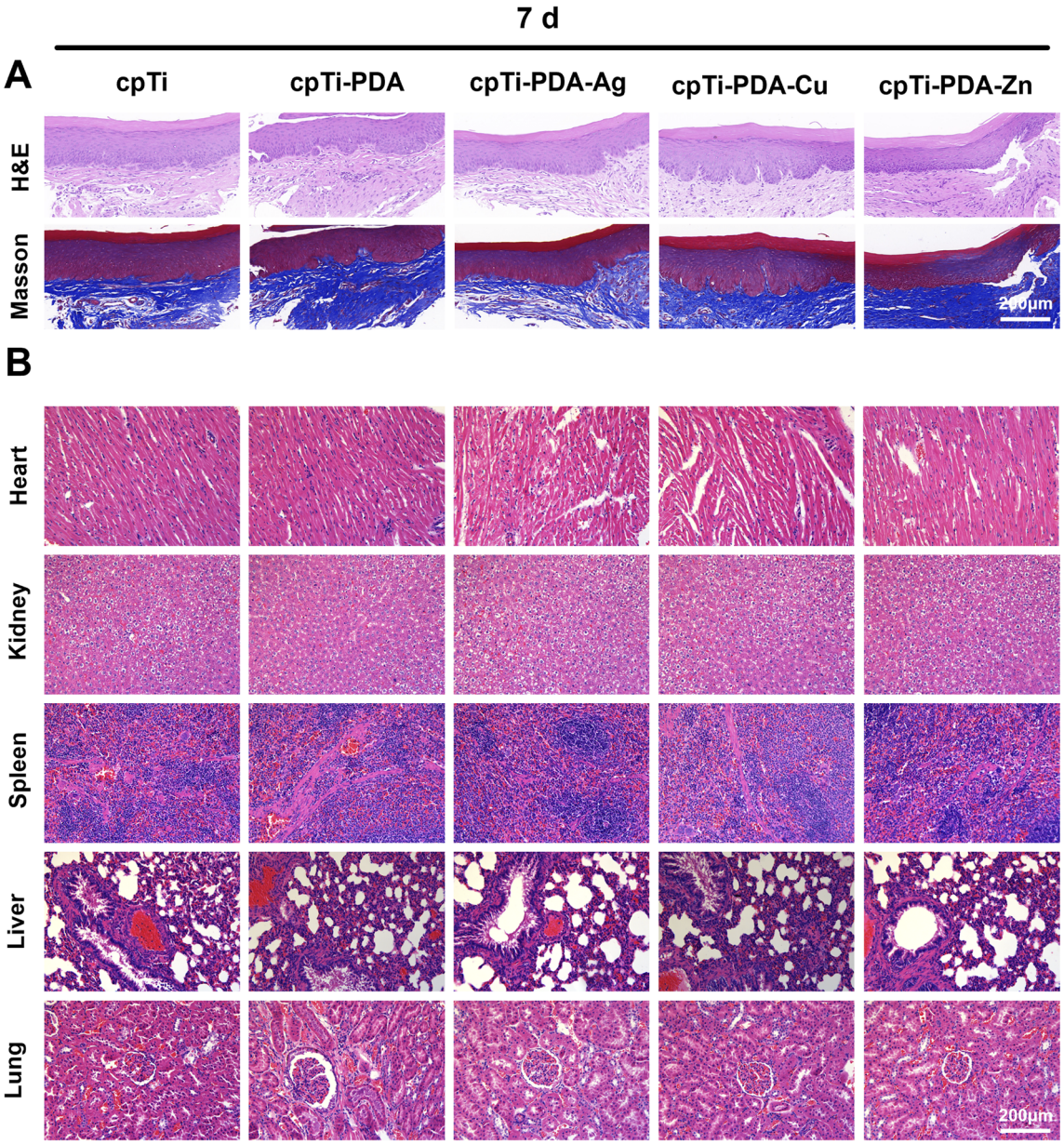

Fig. 7 Evaluation of *in vivo* biocompatibility. (A) Soft tissue of different groups assessed by H&E and Masson's staining. (B) H&E staining images of key organs (heart, kidney, spleen, liver, lung) from various samples.

colony counting and live–dead bacterial staining experiments conducted on samples from each group revealed no significant difference in bacterial inhibition between the cpTi group and the cpTi-PDA group. The observed antibacterial effects of the cpTi-PDA-Ag, cpTi-PDA-Cu, and cpTi-PDA-Zn groups appeared to be primarily attributable to the inherent broad-spectrum antimicrobial properties of the metal ions themselves. These findings necessitated further investigation to validate and elucidate the mechanisms underlying these effects.

3.5. *In vivo* study

Given the inherent complexity of biological systems, the use of animal models is indispensable for validating the safety and efficacy of materials prior to their clinical application. To more accurately simulate the intraoral environment, the placement of implants following the extraction of the maxillary first molar in rats has become a widely adopted methodology. Numerous studies have explored diverse implant designs in this context; for example, E. Blank *et al.* utilized segmental implants in the rat maxilla for preclinical evaluations of implant materials,[58] while T. Koutouzis *et al.* investigated the onset and progression of peri-implant inflammation using intraosseous implants with bonded abutments.[59] In this study, we designed an implant that was specifically tailored to the anatomical characteristics and soft and hard tissue conditions of the rat maxilla. The abutment was engineered to ensure optimal gingival penetration height and contour (Fig. 6A and B). Furthermore, we endeavored to replicate the clinical immediate implant surgical procedure as closely as possible to minimize extraneous influences and postoperative discomfort for the experimental animals (Fig. 6C and D).

Previous studies utilizing animal models have indicated that an epithelial barrier typically begins to develop around the implant within 1 to 2 weeks, characterized by a significant presence of fibroblasts and vascular structures.[60] In this study, we aimed to evaluate early soft tissue healing by collecting peri-implant soft tissue samples one week after post-immediate implant surgery. Fig. 7A showed H&E and Masson's staining of early peri-implant soft tissue sections with connective tissue formation. Comparative analysis of the groups demonstrated no significant differences in histological findings from H&E and Masson's staining, suggesting that the soft tissues exhibited satisfactory healing at this early time point.

Simultaneously, as seen in Fig. 7B, the major metabolic organs of rats from each group were excised and subjected to H&E staining, revealing no pathological abnormalities upon microscopic examination. These results indicated that the materials employed across all groups exhibited satisfactory biosafety *in vivo*. Notably, the biocompatibility of the cpTi-PDA-Ag group displayed divergent outcomes between *in vitro* and *in vivo* assessments, necessitating further investigation and elucidation.

4. Conclusions

In this study, we systematically evaluated the functional performance of titanium surfaces modified with Ag^{+}, Cu^{2+}, and Zn^{2+} *via* a metal-polydopamine (PDA) coordination strategy. Key findings revealed distinct interaction mechanisms and functional outcomes among the three metal ions. XPS/EDS analyses demonstrated that Zn^{2+} and Cu^{2+} predominantly formed coordination complexes with PDA's catechol groups, whereas Ag^{+} was reduced to metallic nanoparticles (Ag^{0}) through redox reactions. This divergence led to contrasting ion-release profiles (Zn^{2+} > Cu^{2+} > Ag^{+}) and biofunctional behaviors. Electrochemical testing under H_2O_2-simulated oxidative stress identified Zn-PDA as the most corrosion-resistant coating, with a polarization resistance of 4330 kΩ cm^2, significantly outperforming Cu-PDA (3900 kΩ cm^2) and Ag-PDA (2850 kΩ cm^2). The Zn-PDA coating retained >80% of PDA's intrinsic antioxidant capacity, while Ag-PDA suffered substantial antioxidant loss due to redox interference.

Antimicrobial assays highlighted Ag-PDA's superior efficacy, achieving >95% reduction against *S. aureus* and *E. coli*, attributed to Ag^{0} nanoparticle release. However, *in vitro* cytotoxicity tests revealed Ag-PDA's adverse effects on L-929 cell proliferation, whereas Zn-PDA and Cu-PDA enhanced cytocompatibility and cell spreading. *In vivo* rat models confirmed excellent biocompatibility across all groups, with no pathological abnormalities in major organs or differences in soft tissue healing, contrasting prior reports of Ag-induced cytotoxicity.

These results highlight the trade-offs among metal-specific properties: Zn-PDA exhibits robust corrosion resistance, antioxidant retention, and biosafety; Cu-PDA demonstrates moderate antimicrobial activity and antioxidant preservation; while Ag-PDA achieves superior antibacterial performance at the expense of antioxidant capacity and cytocompatibility. This comparative analysis provides a design framework for tailoring multifunctional coatings to clinical needs, emphasizing Zn-PDA as a promising candidate for enhancing peri-implant tissue stability under oxidative and microbial challenges.

Data availability

The data that support the findings of this study are available from the corresponding author upon reasonable request.

Author contributions

Yu-kun Mei: conceptualization (equal); data curation (lead); formal analysis (lead); investigation (equal); methodology (equal); writing – original draft (lead). Ya-wen Zhu: formal analysis (equal); investigation (equal); methodology (equal). Yu-wen Wei: investigation (equal); methodology (equal). Shu-di Li: formal analysis (equal); investigation (equal). Xuan Zhou: formal analysis (equal); methodology (equal). Ya-nan Yao: data curation (equal); investigation (equal). Jing Qiu: conceptualization (equal); funding acquisition (lead); project administration (lead); resources (lead); supervision (lead); writing – review & editing (lead).

Conflicts of interest

There are no conflicts to declare.

Acknowledgements

This work was supported by the National Natural Science Foundation of China (Project Number: 82271003), the Natural Science Foundation of Jiangsu Province (Project Number: BK20241865), and the Jiangsu Province Capability Improvement Project through Science, Technology, and Education-Jiangsu Provincial Research Hospital Cultivation Unit (Project Number: YJXYYJSDW4), Jiangsu Provincial Medical Innovation Center (Project Number: CXZX202227).

References

1 H. Wu, X. Chen, L. Kong and P. Liu, *Materials*, 2023, **16**(21), 6860.
2 J. Zhang, Y. Zhuang, R. Sheng, H. Tomás, J. Rodrigues, G. Yuan, X. Wang and K. Lin, *Mater. Horiz.*, 2024, **11**, 12–36.
3 T. Berglundh, A. Mombelli, F. Schwarz and J. Derks, *Periodontol*, 2000, 2024, DOI: **10.1111/prd.12549**.
4 F. Aellos, J. A. Grauer, K. G. Harder, J. S. Dworan, G. Fabbri, P. L. Cuevas, X. Yuan, B. Liu, J. B. Brunski and J. A. Helms, *J. Clin. Periodontol.*, 2024, **51**, 806–817.
5 X. Yuan, X. Pei, J. Chen, Y. Zhao, J. B. Brunski and J. A. Helms, *J. Clin. Periodontol.*, 2021, **48**, 745–753.
6 K. Apaza-Bedoya, M. Tarce, C. A. M. Benfatti, B. Henriques, M. T. Mathew, W. Teughels and J. C. M. Souza, *J. Periodontal Res.*, 2017, **52**, 946–954.
7 E. K. Brooks, S. Der and M. T. Ehrensberger, *Mater. Sci. Eng., C*, 2016, **60**, 427–436.
8 R. Tsaryk, K. Peters, S. Barth, R. E. Unger, D. Scharnweber and C. J. Kirkpatrick, *Biomaterials*, 2013, **34**, 8075–8085.
9 N. Contuzzi, G. Casalino, A. Boccaccio, A. Ballini, I. A. Charitos, L. Bottalico and L. Santacroce, *J. Funct. Biomater.*, 2022, **14**(1), 14.
10 D. A. Siddiqui, L. Guida, S. Sridhar, P. Valderrama, T. G. Wilson, Jr. and D. C. Rodrigues, *J. Periodontol.*, 2019, **90**, 72–81.
11 J.-H. Ahn, H.-S. Kim, K. J. Lee, S. Jeon, S. J. Kang, Y. Sun, R. G. Nuzzo and J. A. Rogers, *Science*, 2006, **314**, 1754–1757.
12 P. Alivisatos, *Nat. Biotechnol.*, 2004, **22**, 47–52.
13 R. Langer, *Science*, 2001, **293**, 58–59.
14 H. Lee, S. M. Dellatore, W. M. Miller and P. B. Messersmith, *Science*, 2007, **318**, 426–430.
15 H. Lee, N. F. Scherer and P. B. Messersmith, *Proc. Natl. Acad. Sci. U. S. A.*, 2006, **103**, 12999–13003.
16 Z. Wang, Y. Zou, Y. Li and Y. Cheng, *Small*, 2020, **16**, e1907042.
17 L. Jia, F. Han, H. Wang, C. Zhu, Q. Guo, J. Li, Z. Zhao, Q. Zhang, X. Zhu and B. Li, *J. Orthop Translat.*, 2019, **17**, 82–95.
18 Y. Zhang, L. Liu, M. Li, S. Wang, J. Fu, M. Yang, C. Yan, Y. Liu and Y. Zheng, *Sci. Rep.*, 2025, **15**, 3063.
19 Q. Liu, H. Li, L. Kong, Y. Du, Y. Da, Z. Sun, Y. Dong, Y. Liu, X. Tian and H. Wang, *Prog. Org. Coat.*, 2024, **197**, 108782.
20 J. Song, H. Liu, M. Lei, H. Tan, Z. Chen, A. Antoshin, G. F. Payne, X. Qu and C. Liu, *ACS Appl. Mater. Interfaces*, 2020, **12**, 8915–8928.
21 L. Tian, C. Chen, J. Gong, Q. Han, Y. Shi, M. Li, L. Cheng, L. Wang and B. Dong, *Sensors*, 2023, **23**(10), 4641.
22 A. Mondal, R. Devine, L. Estes, J. Manuel, P. Singha, J. Mancha, M. Palmer and H. Handa, *J. Colloid Interface Sci.*, 2021, **585**, 716–728.
23 H. Li, Y. Jia, S. Bai, H. Peng and J. Li, *Adv. Colloid Interface Sci.*, 2024, **334**, 103316.
24 T. Odatsu, S. Kuroshima, M. Sato, K. Takase, A. Valanezhad, M. Naito and T. Sawase, *Antibiotics*, 2020, **9**.
25 T. Aissou, J. Jann, N. Faucheux, L.-C. Fortier, N. Braidy and J. Veilleux, *Appl. Surf. Sci.*, 2023, **639**, 158204.
26 M. Jannesari, O. Akhavan, H. R. Madaah Hosseini and B. Bakhshi, *ACS Appl. Mater. Interfaces*, 2020, **12**, 35813–35825.
27 X. Wang, L. Pan, A. Zheng, L. Cao, J. Wen, T. Su, X. Zhang, Q. Huang and X. Jiang, *Bioact. Mater.*, 2023, **24**, 236–250.
28 J. Qiu, W.-Q. Yu, F.-Q. Zhang, R. J. Smales, Y.-L. Zhang and C.-H. Lu, *Eur. J. Oral Sci.*, 2011, **119**(1), 93–101.
29 W.-Q. Zhu, S.-Y. Shao, L.-N. Xu, W.-Q. Chen, X.-Y. Yu, K.-M. Tang, Z.-H. Tang, F.-M. Zhang and J. Qiu, *J. Nanobiotechnol.*, 2019, **17**, 55.
30 F. Wang, W. Ge, T. Shen, B. Ye, Z. Fu and Y. Lu, *Appl. Surf. Sci.*, 2017, **410**, 513–518.
31 M. B. Davidsen, J. F. L. Teixeira, J. Dehli, C. Karlsson, D. Kraft, P. P. C. Souza and M. Foss, *Colloids Surf., B*, 2021, **207**, 111972.
32 A. Bhattacharjee and S. Bose, *Biomater. Adv.*, 2023, **153**, 213487.
33 L. Wang, X. Shang, Y. Hao, G. Wan, L. Dong, D. Huang, X. Yang, J. Sun, Q. Wang, G. Zha and X. Yang, *RSC Adv.*, 2019, **9**, 2892–2905.
34 C. Ding, Y. Lu, M. Xiang, F. Wu, P. Chen, W. Gan, J. Guo, J. Li, Q. Ling, Z. Zhao, L. Chen, M. Zhang and Z. Sun, *J. Colloid Interface Sci.*, 2023, **646**, 275–289.
35 H. Huang, X. Sha, Y. Cui, S. Sun, H. Huang, Z. He, M. Liu, N. Zhou, X. Zhang and Y. Wei, *J. Colloid Interface Sci.*, 2020, **567**, 190–201.
36 W. Wang, Y. Jiang, S. Wen, L. Liu and L. Zhang, *J. Colloid Interface Sci.*, 2012, **368**, 241–249.
37 Y. Ding, L.-T. Weng, M. Yang, Z. Yang, X. Lu, N. Huang and Y. Leng, *Langmuir*, 2014, **30**, 12258–12269.
38 F. Schwarz, M. Herten, M. Sager, M. Wieland, M. Dard and J. Becker, *Clin. Oral Invest.*, 2007, **11**, 245–255.
39 X.-Y. Yu, W.-Q. Zhu, W. Chen, W.-Q. Chen, S.-M. Zhang and J. Qiu, *Mater. Sci. Eng., C*, 2021, **119**, 111610.
40 Y. Duan, Y. Wu, R. Yan, M. Lin, S. Sun and H. Ma, *Int. J. Biol. Macromol.*, 2021, **184**, 109–117.
41 J. C. Souza, S. L. Barbosa, E. A. Ariza, M. Henriques, W. Teughels, P. Ponthiaux, J. P. Celis and L. A. Rocha, *Mater. Sci. Eng., C*, 2015, **47**, 384–393.
42 Y. Ye, L. Zheng, T. Wu, X. Ding, F. Chen, Y. Yuan, G. C. Fan and Y. Shen, *ACS Appl. Mater. Interfaces*, 2020, **12**, 35626–35637.
43 H. Liu, X. Qu, H. Tan, J. Song, M. Lei, E. Kim, G. F. Payne and C. Liu, *Acta Biomater.*, 2019, **88**, 181–196.
44 Z. Li, X. Shan, Z. Chen, N. Gao, W. Zeng, X. Zeng and L. Mei, *Adv. Sci.*, 2020, **8**, 2002589.

45 M. Nasr Azadani, A. Zahedi, O. K. Bowoto and B. I. Oladapo, *Prog. Biomater.*, 2022, **11**, 1–26.
46 R. I. M. Asri, W. S. W. Harun, M. Samykano, N. A. C. Lah, S. A. C. Ghani, F. Tarlochan and M. R. Raza, *Mater. Sci. Eng., C*, 2017, **77**, 1261–1274.
47 N. Singh, U. Batra, K. Kumar, N. Ahuja and A. Mahapatro, *Bioact. Mater.*, 2023, **19**, 717–757.
48 L. Wei and Z. Gao, *RSC Adv.*, 2023, **13**, 8427–8463.
49 Y. Zhang, K. Gulati, Z. Li, P. Di and Y. Liu, *Nanomaterials*, 2021, **11**(10), 2489.
50 M. K. Yazdi, M. Zare, A. Khodadadi, F. Seidi, S. M. Sajadi, P. Zarrintaj, A. Arefi, M. R. Saeb and M. Mozafari, *ACS Biomater. Sci. Eng.*, 2022, **8**, 2196–2219.
51 K. Guo, Y. Wang, Z. X. Feng, X. Y. Lin, Z. R. Wu, X. C. Zhong, Z. M. Zhuang, T. Zhang, J. Chen and W. Q. Tan, *Int. J. Nanomed.*, 2024, **19**, 859–881.
52 T. Guo, K. Gulati, H. Arora, P. Han, B. Fournier and S. Ivanovski, *Dent. Mater.*, 2021, **37**, 816–831.
53 L. Su, Y. Yu, Y. Zhao, F. Liang and X. Zhang, *Sci. Rep.*, 2016, **6**, 24420.
54 L. Han, P. Li, P. Tang, X. Wang, T. Zhou, K. Wang, F. Ren, T. Guo and X. Lu, *Nanoscale*, 2019, **11**, 15846–15861.
55 Y. Ye, L. Zheng, T. Wu, X. Ding, F. Chen, Y. Yuan, G.-C. Fan and Y. Shen, *ACS Appl. Mater. Interfaces*, 2020, **12**, 35626–35637.
56 H. Liu, X. Qu, H. Tan, J. Song, M. Lei, E. Kim, G. F. Payne and C. Liu, *Acta Biomater.*, 2019, **88**, 181–196.
57 Z. Li, X. Shan, Z. Chen, N. Gao, W. Zeng, X. Zeng and L. Mei, *Adv. Sci.*, 2020, **8**, 2002589.
58 E. Blank, J. Grischke, A. Winkel, J. Eberhard, N. Kommerein, K. Doll, I. Yang and M. Stiesch, *BMC Oral Health*, 2021, **21**, 313.
59 T. Koutouzis, C. Eastman, S. Chukkapalli, H. Larjava and L. Kesavalu, *J. Periodontol.*, 2017, **88**, e32–e41.
60 T. Berglundh, I. Abrahamsson, M. Welander, N. P. Lang and J. Lindhe, *Clin. Oral Implants Res.*, 2007, **18**, 1–8.